Supplementary Information

Edge Contact for Carrier Injection and Transport in MoS_2 Field-Effect Transistors

Homin Choi[†,‡], Byoung Hee Moon[†,*], Jung Ho Kim[†,‡], Seok Joon Yun[†,‡], Gang Hee Han[†], Sung-gyu Lee[†,‡], Hamza Zad Gul[†,‡], Young Hee Lee[†,‡,*]

[†]Center for Integrated Nanostructure Physics, Institute for Basic Science, Sungkyunkwan University, Suwon 16419, Korea

[‡]Department of Energy Science, Department of Physics, Sungkyunkwan University, Suwon 16419, Korea

Supplementary Note 1. EDS mapping image obtained *via* cross-sectional transmission electron microscopy (TEM) and X-ray photoelectron spectroscopy (XPS) and measurements for Mn and Mn/Au films.

In order to check the oxidation problem in our vacuum condition, $10^{-6}\sim10^{-7}$ torr, for the metal deposition, we prepared a series of samples for energy dispersive spectrometry (EDS) mapping by cross-section TEM and for the X-ray photoelectron spectroscopy (XPS) measurements. For the case of TEM, Fig. S1(a) shows EDS mapping image of 10 nm-thick edge contacted MoS_2 device with Mn/Au (10 nm / 60 nm). It is clear that Mn makes a major contact to the edge of MoS_2 and the top surface of the bottom BN whose portion remains unetched. One notable thing is that the rich Mn atoms diffuse into the Au region. Next, we note the two things in Fig. S1(a). First, the number of Oxygen atoms decreases gradually from bottom (Mn metal) to top (Au metal). Second, Mn atoms highly outnumber oxygen atoms in the region of interest. These two results imply that Mn is partially oxidized near the junction.

To confirm further with XPS measurement with a few nm thick Au deposition, we prepared 4 samples; i.e., first 15 nm-thick Mn film, and next three samples having different Au thickness from 1 to 5 nm deposited on top of 15 nm-thick Mn film for passivation *in situ* within the chamber. All samples were exposed to the air after the metal deposition, and XPS was measured. In Fig. S1(b), we show four samples, only Mn and Mn with 1, 3, and 5 nm-thick Au on the top. All samples share very similar features. We note that the bare Mn metal is still preserved with a metal peak around 638.9 eV. Mn atoms are partially oxidized by the native oxides as a clear signature of MnO satellite peak near 647 eV. Pure Mn atoms are still observed even at further deposition of Au up to 5 nm Fig. S1(b). Au deposition at lower thickness like 1 nm could be agglomerated to nanoparticles.

In general, MnO has a cubic rock salt structure. In this case, it shows the insulating behavior with ~ 3.9 eV band gap for the antiferromagnetic phase[1, 2]. Still, our experimental results for the devices with both Mn-top and -edge contacts exhibit the relatively high output current and dominant n-type characteristics, implying the dominant presence of Mn metal. We believe that pure Mn plays a major role for the charge injection at the interface. The similar result was reported for Cr, highly feasible to the partial oxidation of Cr metal, which is preserved at the interface of Cr and MoS_2.[3]

We conclude that even at a few nm-thin Au, Mn could be partially oxidized in the worst scenario but pure Mn metal is still preserved, and in our case of 60 nm-thick Au, pure Mn metal is well dominantly preserved in our device

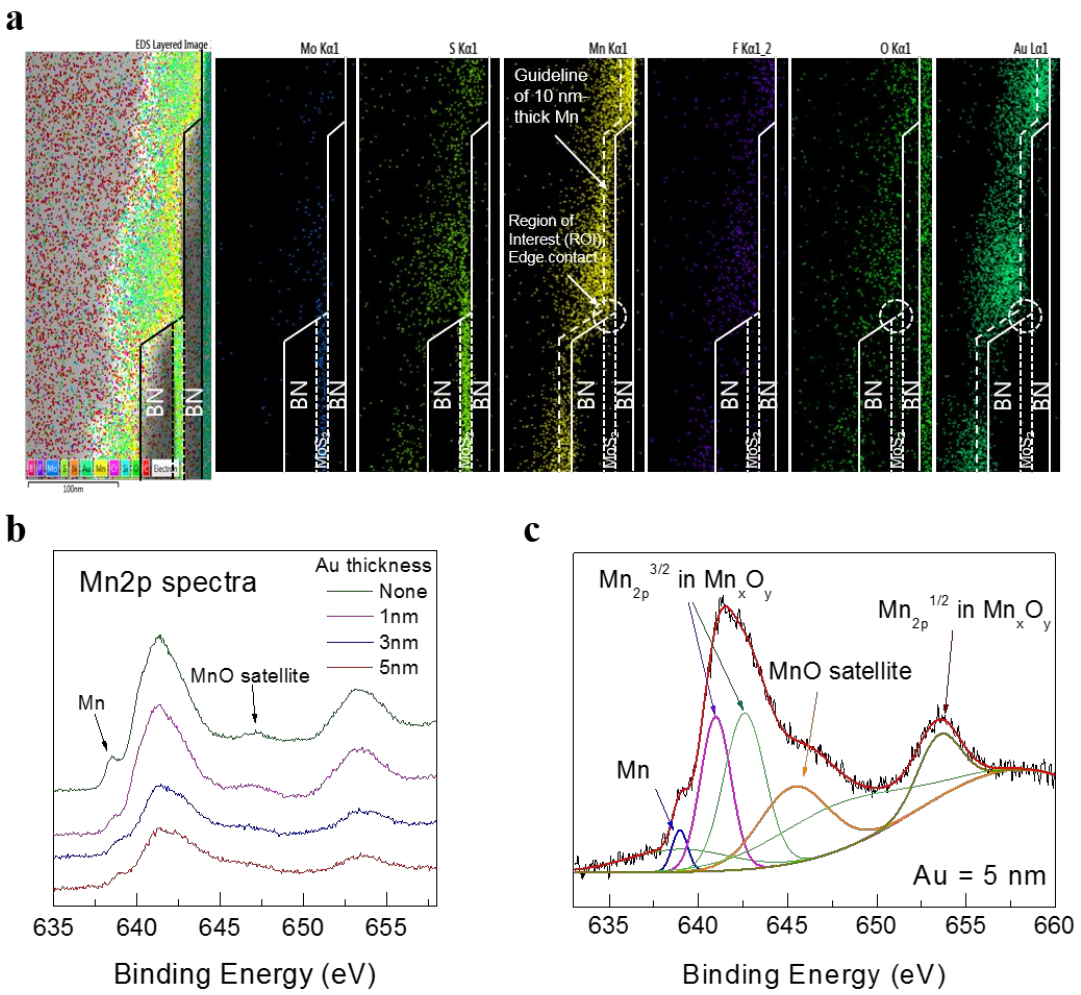

Fig. S1. (a) EDS mapping image by cross-section TEM for 10 nm-thick edge contacted device with Mn. (b) XPS spectra of Mn2p for various Au thickness on 15 nm-thick Mn. (c) XPS spectra of Mn2p for the sample of 5 nm-thick Au film on Mn.

Supplementary Figure 2. I_{DS}–V_{BG} characteristics of TCMs of Mn and Au contacts.

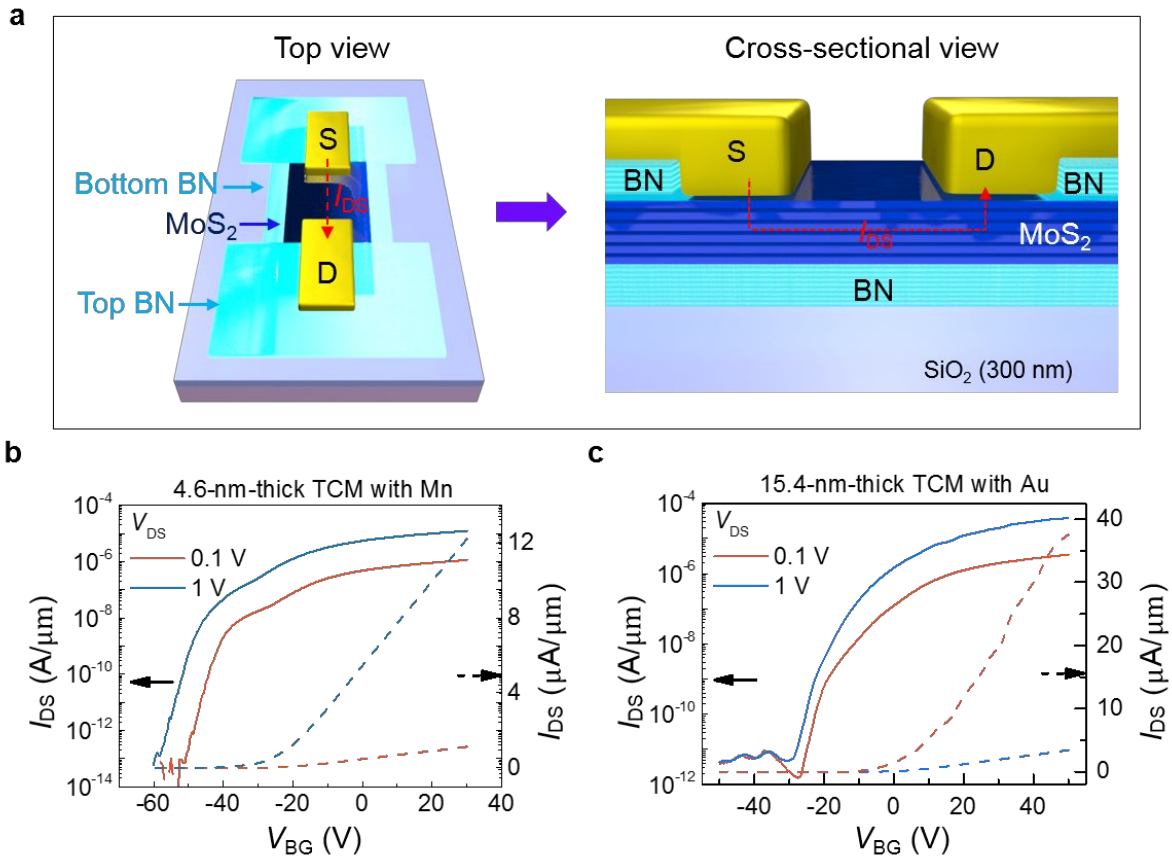

Fig. S2. I_{DS}–V_{BG} characteristics of TCMs of Mn and Au contacts. (a) Schematic of the top-contacted multilayer MoS_2. (b, c) I_{DS} vs. V_{BG} characteristics for TCM with Mn (b) and TCM with Au (c) for selected drain voltages at room temperature.

Supplementary Note 2. Annealing effect on I_{DS}-V_{BG} characteristics of ECM with Au.

The transfer characteristics of devices are often changed after annealing. To see this effect, we fabricated ~12 nm-thick MoS_2 device with Au-edge contacts, and measured the transfer characteristic before and annealing. Annealing was performed at 150 ˚C for 2 hours in high vacuum. As shown in Fig. S3, the hole transport is suppressed while electron transport is enhanced after annealing. Thus, the dominant carrier transport, either holes or electrons, in transfer characteristics does not come exclusively from the thickness issue. We suspect that the fluctuation in transfer characteristics can occur due to the different contact or channel quality, which likely occurs during the device fabrication.

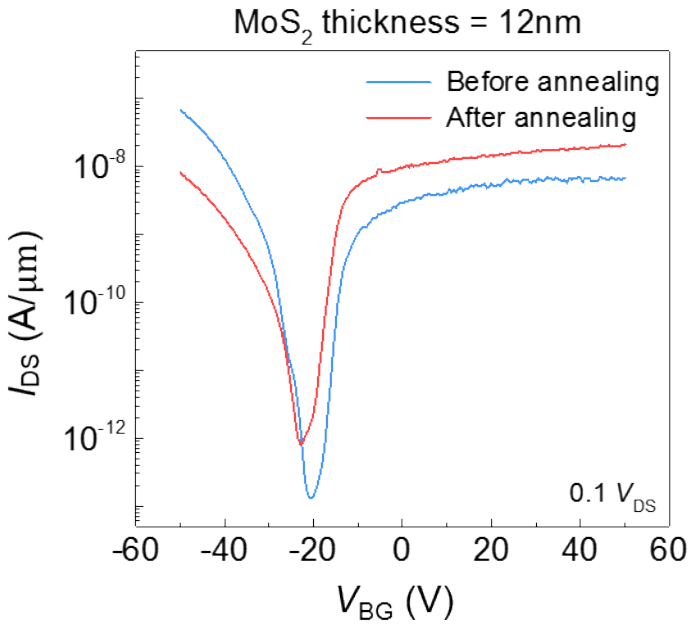

Fig. S3. I_{DS}-V_{BG} characteristics of ~ 12 nm-thick MoS_2 devices with Au-edge contacts, measured at V_{DS} = 0.1 V. Annealing was performed at 150˚C for 2 hours in High vacuum.

Supplementary Figure 4. I_{DS}–V_{BG} characteristics of ECM with Cr

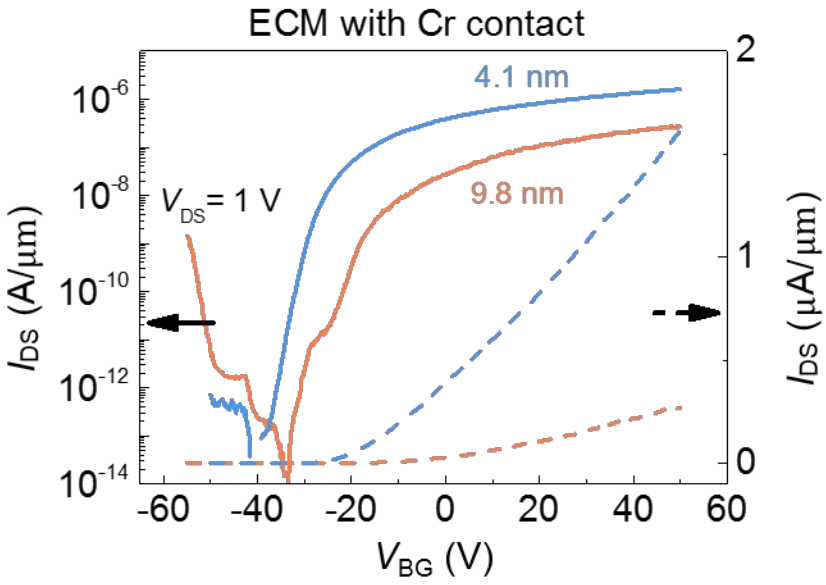

Fig. S4. I_{DS}–V_{BG} characteristics of ECM with Cr. I_{DS}-V_{BG} characteristics of ECM with Cr with different flake thicknesses. The thicker device (9.8 nm-thick) shows weak ambipolar characteristics.

Supplementary Note 3. Calculation of band-bending profiles of MoS_2 modulated by the dipole pinning charges for the Au contact depending on the contact geometry; ECM/TCM, and carrier concentration.

We calculate the final band bending profile, $V_{\mathrm{Final}}(\mathrm{x})$, at the junction by summing the electrostatic potential curve, $V_{\mathrm{ideal}}(\mathrm{x})$, derived from Poisson's equation, and the dipole potential curve, $V_{\mathrm{Dipole}}(\mathrm{x,\ t})$, at the interface between Au and MoS_2,

$$V_{\mathrm{Fianl}}(\mathrm{x})\ [\mathrm{V}] = V_{\mathrm{ideal}}(\mathrm{x}) + V_{\mathrm{Dipole}}(x, t)\ \ [\mathrm{V}] \quad (1)$$

where x is the displacement from the interface at junction toward MoS_2 channel. Poisson's equation can be phenomenologically approximated for ECM and TCM with Au as,[4]

$$\mathrm{q}V_{\mathrm{ideal}}(\mathrm{x})\ [\mathrm{eV}] = \mathrm{q}V_{\mathrm{P}}\frac{(\mathrm{x} - W_{\mathrm{dmax}})^2}{{W_{\mathrm{dmax}}}^2} + (E_{\mathrm{C}} - E_{\mathrm{F}})\ [\mathrm{eV}],\ \ \mathrm{x} \le W_{\mathrm{d}} \quad (2)$$

Here, $\mathrm{q}V_{\mathrm{P}}$ is the contact potential,

$$\mathrm{q}V_{\mathrm{P}}\ [\mathrm{eV}] = (\phi_{\mathrm{m}} - \chi) - (E_{\mathrm{C}} - E_{\mathrm{F}})\ [\mathrm{eV}] \quad (3)$$

For $\phi_{\mathrm{m}} - \chi$, $\phi_{\mathrm{m}} = 5.1$ eV for work function of Au and $\chi = 4.0$ eV for electron affinity of MoS_2.[5] $E_{\mathrm{C}} - E_{\mathrm{F}}$ is energy difference between conduction band minimum and Fermi-level of MoS_2 in the channel region of MoS_2. We used $E_{\mathrm{C}} - E_{\mathrm{F}} = 0.1$ eV for n-doped multilayer MoS_2 and $E_{\mathrm{C}} - E_{\mathrm{F}} = 0.6$ eV for intrinsic multilayer MoS_2. W_{dmax} is the maximum depletion width in MoS_2 and,

$$W_{\mathrm{dmax}} = \sqrt{\frac{2\varepsilon_{\mathrm{MoS_2}}V_{\mathrm{P}}}{\mathrm{q}N_{\mathrm{3D}}}} \quad (4)$$

Where, $\varepsilon_{\mathrm{MoS_2}}$ is the permittivity of MoS_2, and it ranges from 4 to 10 depending on sample thickness.[6] n_{3D} are the carrier density in three-dimension (3D).

Pinning charges are modelled as a dipole in two-parallel rectangular contact width (W) × sample thickness (t) for ECM and contact width (W) × transfer length (l_{TL}) for TCM with a separation of d. We choose material thickness, $t = 10$ nm, $l_{\mathrm{TL}} = 1$ μm, and $W = \infty$. Then, the energy of dipole potential toward MoS_2 channel (x- and y-axis) by pinning dipole charges, $\mathrm{q}V_{\mathrm{Dipole}}(x, t)$, can be expressed as,

$$\mathrm{q}V_{\mathrm{Dipole}}(x, t)\ [\mathrm{eV}] = -\mathrm{q}\left(\int_{-\frac{d}{2}}^{x} E \cdot \mathrm{d}x + \int_{+\frac{d}{2}}^{x} E \cdot \mathrm{d}x\right)[\mathrm{eV}] \quad (5)$$

where, $E(x)$ is the electric field due to dipole sheet along the x-axis expressed as,

$$E(x) = \frac{\sigma x}{4\pi\varepsilon_{MoS_2}} \int_{-w/2}^{w/2} \int_{-t/2}^{t/2} \frac{dydz}{(x^2 + y^2 + z^2)^{3/2}} \quad (6)$$

where, σ is the pinning charge density on dipole sheet, and can be expressed in terms of the number of pinning charges per a single sulphur atom; n_e can be represented as,

$$\sigma_E = \frac{4q}{a \cdot c} \times n_e = 1.7 \left[\frac{C}{m^2}\right] \times n_e \text{ for edge contact} \quad (7)$$

$$\sigma_T = \frac{q}{a \cdot \frac{\sqrt{3}}{2}a} \times n_e = 1.9 \left[\frac{C}{m^2}\right] \times n_e \text{ for top contact} \quad (8)$$

where, $a \cdot c$ in Eq. S7 is the unit surface which contains four-sulphur atoms for ECM and $a \cdot \frac{\sqrt{3}}{2}a$ in Eq. S8 is the unit surface which contains a single of sulphur atom for TCM. The lengths are $a = 0.31$ nm, $c = 1.21$ nm.[7] For this purpose, we choose $d = 0.32$ nm.[6]

Supplementary Figure 5. Band-bending plot for the intrinsic ECM with respect to the distance from the contact to the MoS_2 channel with an increasing n_e

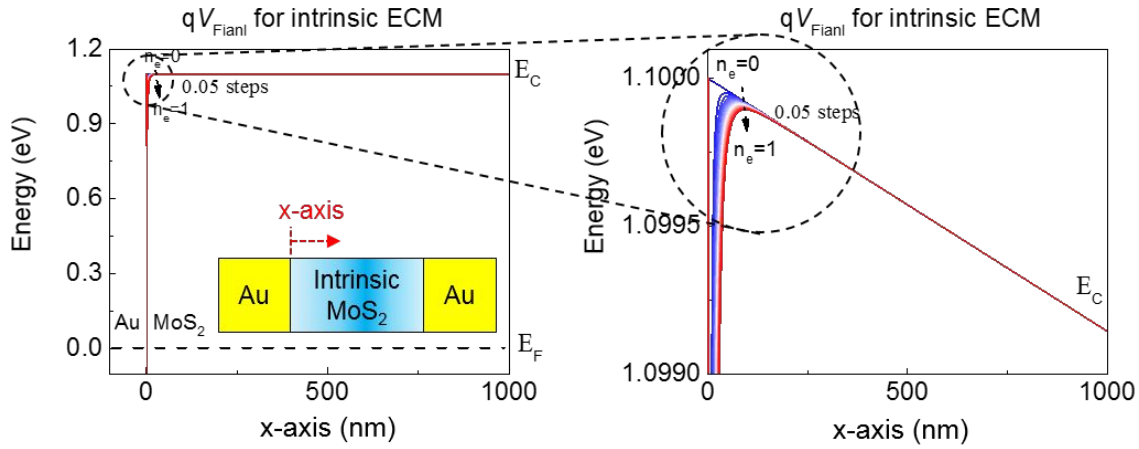

Fig. S5. Band bending plot for intrinsic ECM as a function of distance from contact to MoS_2 channel with increasing n_e. Band bending plot for intrinsic ECM as a function of distance from the contact with increasing n_e. The Fermi-level pinning is almost negligible owing to the large depletion width.

Supplementary Figure 6. Band-bending plots for the TCM and ECM with respect to the distance from the contact to the MoS_2 channel with an increasing n_e.

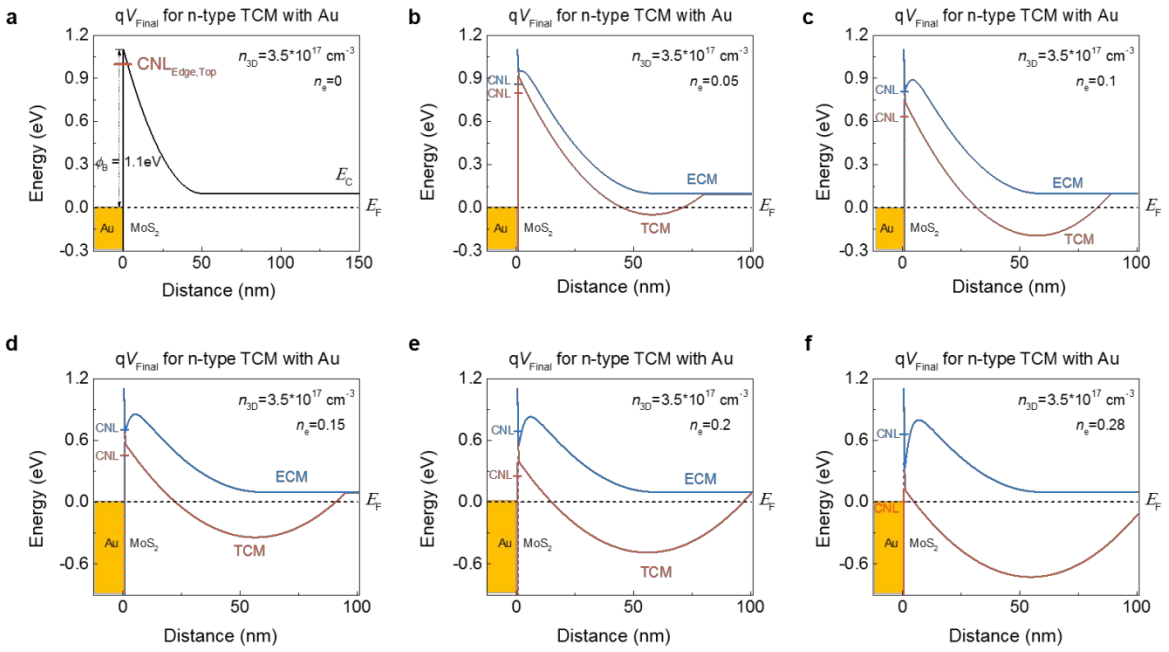

Fig. S6. The band bending plots for TCM and ECM as a function of distance from contact to MoS_2 channel with increasing n_e. (a-f) Band bending plots for ECM (blue curve) and TCM (red curve) with different n_e values from 0 (a) to 0.28 (f). As n_e, increases, Schottky barrier height decreases toward to charge-neutrality level, i.e., Fermi-level pinning effect is stronger. Particularly, perfect Fermi-level pinning for TCM (red curve) occurs at $n_e = 0.28$ (f).

Supplementary Note 4. Fermi-level pinning in the TCM for various values of L_T.

The transfer length is determined as $L_T = \sqrt{\rho_{ct}/\rho_{sh}}$, where ρ_{ct} is the contact resistivity and ρ_{sh} is the sheet resistivity of MoS_2 in the contact with a metal. Thus, in general, the better the contact quality is, the shorter the transfer length is. Of course, L_T is also the function of ρ_{sh}. Thus, the reliable determination of L_T is not a trivial task. In previous report, $L_T \sim 40$ nm has been extracted, in which the contact quality has been improved with a metal deposition in a ultra-high vacuum ($\sim 10^{-9}$ torr).

As we show in Fig. S7, the FLP effect is in a slight change with L_T down to 100 nm (Fig. S7 (a) and S7 (b)), but its change becomes noticeable for $L_T \sim 40$ nm (Fig. S7 (c)). This change appears apparently in the resultant peak of the Schottky barrier height as a function of n_e, as shown in Fig. S7 (d). So, the FLP effect becomes weaker with $L_T \sim 40$ nm for the same n_e. However, we note that we would expect higher charge transfer for the better contact, compromising the FLP effect.

More importantly, as we argue in the manuscript, the FLP effect is highly dependent on the doping level. As it is more doped, the depletion width is narrower, allowing easier modulation of the Schottky barrier by pinning charges, and thus stronger FLP occurs. This is the reason most MoS_2 with top contacts exhibit n-type characteristics, i.e., the top surface of MoS_2 exposed to the air is highly n-doped.[8] From this result, we also argued in the conclusion of the manuscript that if the top surface of MoS_2 is kept from the extrinsic doping so that it is close to the intrinsic, the type conversion in MoS_2 with top contact would be possible.

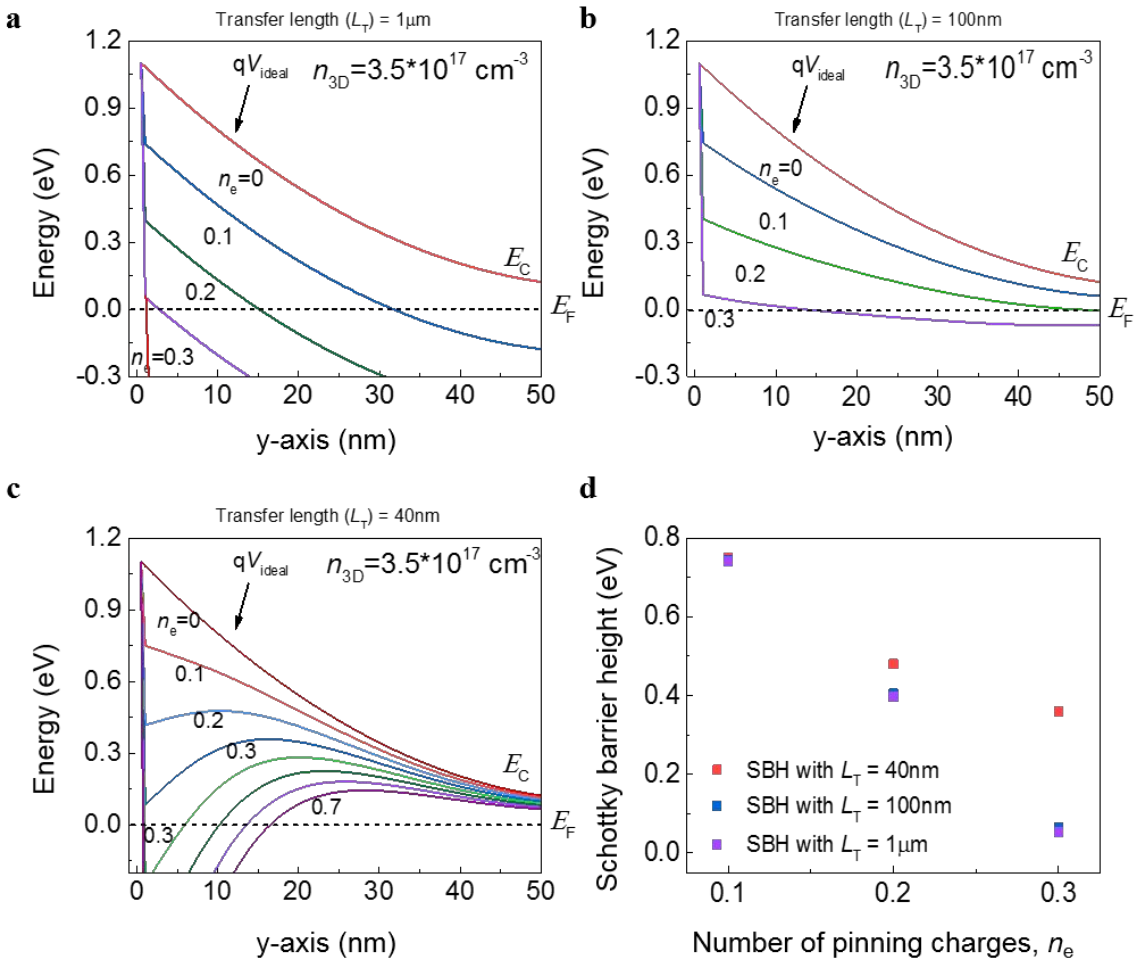

Fig. S7. (a-c) V_{final} at various n_e and $n_{3D} = 3.5 \times 10^{17}$ cm^3 for TCM of L_T = 1 μm, 100 nm, and 40 nm, respectively. (d) Schottky barrier heights determined from the potential peaks as a function of n_e for L_T = 1 μm, 100 nm, and 40 nm.

Supplementary Figure 8. Extraction of the Schottky barrier height for monolayer-thick ECM with Au

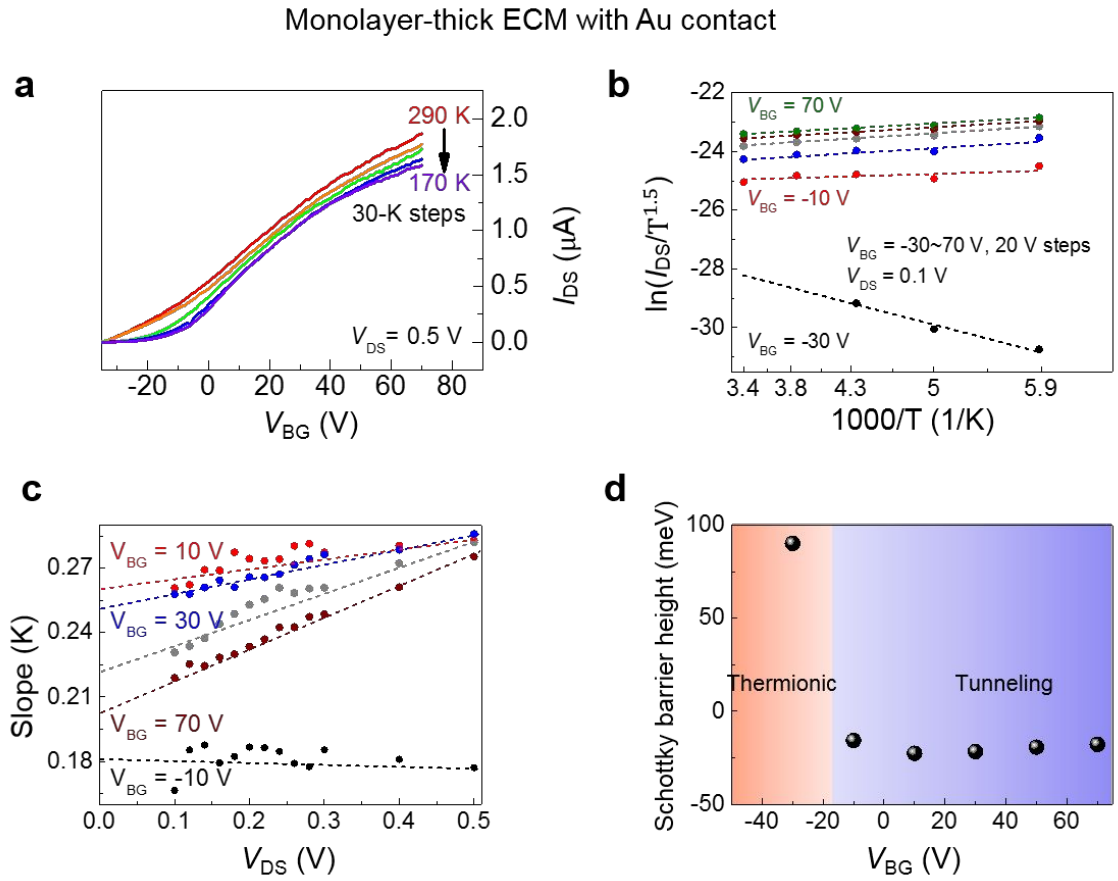

Fig. S8. Extraction of the Schottky barrier height for monolayer-thick ECM with Au. Extraction of the Schottky barrier height for monolayer ECM with Au from thermionic emission theory and Arrhenius plot. (a) Transfer characteristics at V_{DS} = 0.1 with different temperatures. (b) An arrhenius plot $\ln(I_{DS}/T^{3/2})$ vs $1000/T$, for various gate biases V_{BG}. (c) Extraction of ϕ_B *via* the y-intercept values, i.e., zero V_{DS} limit. (d) Obtained Schottky barrier heights ϕ_B as a function of gate bias. Only n-type characteristics is observed because of sizable Fermi-level pinning effect in monolayer MoS_2. Obtained Schottky barrier heights shows a similar trend in Fig.4

Supplementary Figure 9. Contact resistivity of a 4.6-nm-thick ECM with Mn as a function of the gate bias

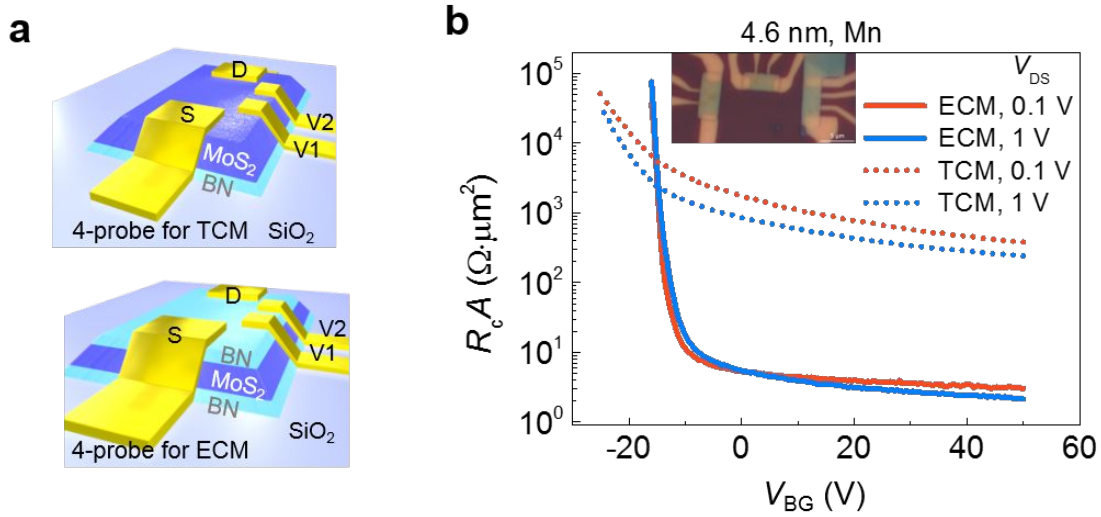

Fig. S9. Contact resistivity of 4.6 nm-thick ECM with Mn as a function of gate bias. (a) Schematics of four-probe measurement for ECM (above) and TCM (below). (b) Contact resistivity for ECM and TCM as a function of gate bias. Contact resistivity of ECM is significantly smaller than that of TCM. Inset is the device image; ECM (left) and TCM (right). Dimension for ECM and TCM: Width for ECM; 2.4 μm. Length (thickness) for ECM; 4.6 nm. Width for TCM; 2.2 μm. Length (Transfer length) for TCM; 1 μm.

Supplementary Figure 10. Schematic of the device fabrication process and optical images of the ECM

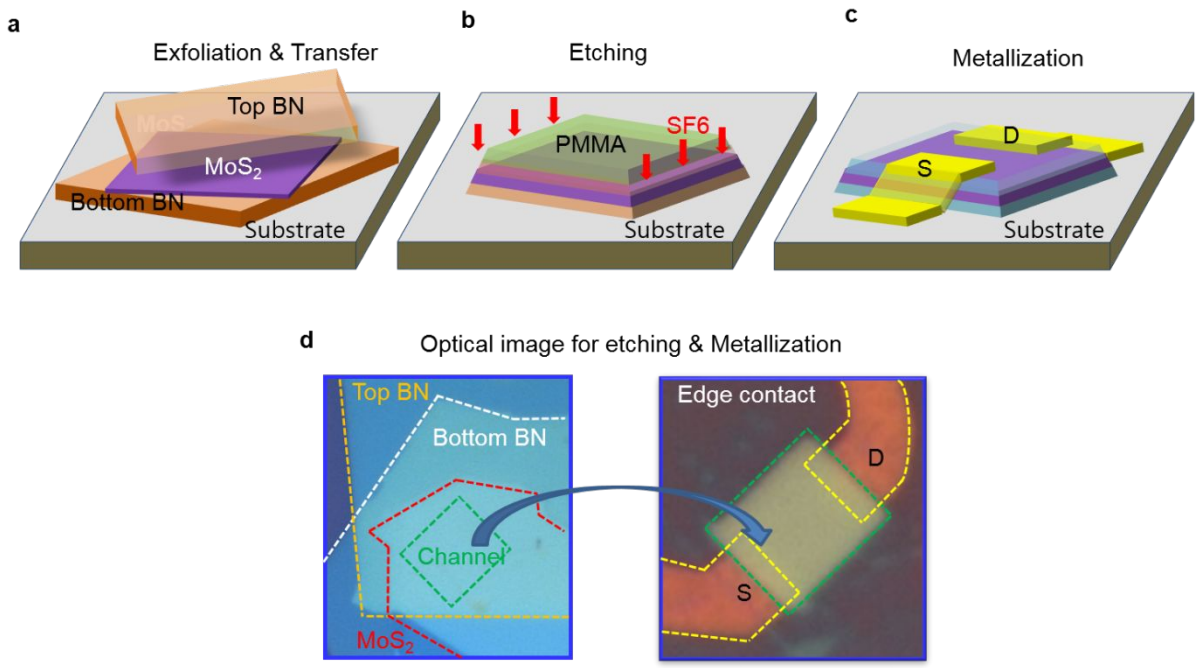

Fig. S10. Schematic device fabrication process and optical images of ECM. (a-c) Schematic of fabrication steps. (a) Stacking heterostructure of h-BN-MoS2-h-BN by using a conventional dry transfer method. (b) SF6 plasma etching for the edge contact. (c) Electrode deposition. (d) The optical image sample (left) and final device (right)

REFERENCES

(1) Van Elp, J.; Potze, R.; Eskes, H.; Berger, R.; Sawatzky, G. Electronic Structure of MnO. *Phys. Rev. B* **1991**, *44,* 1530.

(2) Tran, F.; Blaha, P. Accurate Band Gaps of Semiconductors and Insulators with a Semilocal Exchange-Correlation Potential. *Phys. Rev. Lett.* **2009**, *102*, 226401.

(3) Smyth, C. M.; Addou, R.; McDonnell, S.; Hinkle, C. L.; Wallace, R. M. Contact Metal–MoS_2 Interfacial Reactions and Potential Implications on MoS_2-Based Device Performance. *J. Phys. Chem. C* **2016**, *120*, 14719-14729.

(4) Moon, B. H.; Han, G. H.; Kim, H.; Choi, H.; Bae, J. J.; Kim, J.; Jin, Y.; Jeong, H. Y.; Joo, M. K.; Lee, Y. H.; Lim, S. C. Junction-Structure-Dependent Schottky Barrier Inhomogeneity and Device Ideality of Monolayer MoS_2 Field-Effect Transistors. *ACS Appl. Mater. Interfaces* **2017**, *9*, 11240-11246.

(5) Han, S. W.; Kwon, H.; Kim, S. K.; Ryu, S.; Yun, W. S.; Kim, D. H.; Hwang, J. H.; Kang, J. S.; Baik, J.; Shin, H. J.; Hong, S. C. Band-Gap Transition Induced by Interlayer van der Waals Interaction in MoS_2. *Phys. Rev. B* **2011**, *84*, 045409.

(6) Chen, X. L.; Wu, Z. F.; Xu, S. G.; Wang, L.; Huang, R.; Han, Y.; Ye, W. G.; Xiong, W.; Han, T. Y.; Long, G.; Wang, Y.; He, Y. H.; Cai, Y.; Sheng, P.; Wang, N. Probing the Electron States and Metal-Insulator Transition Mechanisms in Molybdenum Disulphide Vertical Heterostructures. *Nat. Commun.* **2015**, *6*, 6088.

(7) Molina-Sanchez, A.; Wirtz, L. Phonons in Single-Layer and Few-Layer MoS_2 and WS_2. *Phys. Rev. B* **2011**, *84*, 155413.

(8) Siao, M. D.; Shen, W. C.; Chen, R. S.; Chang, Z. W.; Shih, M. C.; Chiu, Y. P.; Cheng, C. M. Two-Dimensional Electronic Transport and Surface Electron Accumulation in MoS_2. *Nat. Commun.* **2018**, *9*, 1442.